PAN POLSKA AKADEMIA NAUK

METROLOGY AND MEASUREMENT SYSTEMS

Index 330930, ISSN 0860-8229

www.metrology.pg.gda.pl

M&MS

ESTIMATION OF SMALL UAV POSITION AND ATTITUDE WITH RELIABLE IN-FLIGHT INITIAL ALIGNMENT FOR MEMS INERTIAL SENSORS

Dingjie Wang[1)], Yi Dong[1)], Qingsong Li[1)], Jie Wu[1)], Yulei Wen[2)]

1) *National University of Defense Technology, College of Aerospace Science and Engineering, Changsha, China* (*wangdingjie11@nudt.edu.cn*, *dongyi13@nudt.edu.cn*, *liqingsong10@nudt.edu.cn*, ✉ *wujie_nudt@sina.com*, +86 0731 8457 3139)

2) *61206 PLA Troop, Beijing, China* (*narutosakula@126.com*)

Abstract

The advance of MEMS-based inertial sensors successfully expands their applications to small *unmanned aerial vehicles* (UAV), thus resulting in the challenge of reliable and accurate in-flight alignment for airborne MEMS-based *inertial navigation system* (INS). In order to strengthen the rapid response capability for UAVs, this paper proposes a robust in-flight alignment scheme for airborne MEMS-INS aided by *global navigation satellite system* (GNSS). Aggravated by noisy MEMS sensors and complicated flight dynamics, a rotation-vector-based attitude determination method is devised to tackle the in-flight coarse alignment problem, and the technique of innovation-based robust Kalman filtering is used to handle the adverse impacts of measurement outliers in GNSS solutions. The results of flight test have indicated that the proposed alignment approach can accomplish accurate and reliable in-flight alignment in cases of measurement outliers, which has a significant performance improvement compared with its traditional counterparts.

Keywords: MEMS, INS, GNSS, in-flight alignment, unmanned aerial vehicle.

1. Introduction

As a small powered aerial vehicle without airborne pilots, UAV has a significant potential in the applications such as scientific research, public security, traffic surveillance, aerial mapping, and disaster rescues [1]. Among all the techniques enabling intelligent flight in harsh environments, an autonomous navigation system is indispensable for individual UAVs. However, traditional *inertial navigation systems* (INS) cannot be suitable for small UAVs due to their big weight, large size and high cost. The advent of cost-effective miniaturized INS, *i.e. Micro-Electro-Mechanical System* (MEMS), enables to use an affordable GNSS/INS integrated system for small UAVs [2]. Its adoption spares more space and weight for other functional instruments, resulting in reinforcement of UAV capability for diverse tasks [3].

Accurate initial position, velocity and attitude are essential for the navigation calculation of a dead reckoning system such as INS. The process whereby the initial navigation state is determined is termed as the initial alignment. Among them, initial position and velocity are easy to obtain with GNSS, but initial attitude is difficult to achieve for a moving body. For an initial

Article history: received on Mar. 04, 2018; accepted on Jun. 14, 2018; available online on Sep. 30, 2018, DOI: 10.24425/123904.

alignment algorithm, the major task is actually to acquire the initial attitude. However, traditional initial alignment algorithms for high-precision INS cannot be simply applied to MEMS-based INS [4, 5]. This is because MEMS-based gyros cannot sense the Earth rate (about 15deg/h) with noise levels of 10–100 deg/h or more. For noisy MEMS-INS, the conventional coarse alignment based on the gravity and Earth rate measurements cannot be accomplished; neither does the self-alignment based on gyro-compassing [6]. A promising solution seems to be an in-motion alignment technique. However, accurate and reliable in-motion alignment still faces difficulty, due to severe model nonlinearity and unpredictable GNSS outliers.

The INS model nonlinearity is mainly caused by uncertain initial attitude errors. The *unscented Kalman filter* (UKF) and *Cubature Kalman filter* (CKF) could be used to tackle the model nonlinearity [4, 7–9]. Superior performance could be achieved by a single UKF without model switches or linearization, but the enormous computation burden deteriorates the real-time property. Moreover, the linearized model can be derived using the trigonometric functions of wander angle for in-flight coarse alignment under large heading errors [5, 10]. Although the reduced computation load meets real-time navigation, this scheme suffers from model inconsistency and weak observability of the trigonometric function error states. Another effective method to reduce the linearized error is to obtain proper initial attitude estimates, meaning the coarse alignment should provide sound initial values [6]. The initial attitude could be derived as the iterative solution for the equivalent optimization problem of finding the minimum eigenvector [11, 12]. In addition, the approximately analytical solution to initial attitude could be also derived with some assumed constraints [13, 14]. However, these approaches are easily affected by either sudden manoeuvres or sideslips.

Besides, outliers may occur in GNSS challenging environments, which would violate the assumed GNSS error model. Thus, the alignment performance will also be deteriorated due to this model mismatch. The Huber-based robust M estimation could be employed to relieve the effects of outlying observations [15, 16]. Sensitive to the initial value, these robust methods may also fail when an outlier occurs in the satellite which affects the satellite geometry significantly [17]. An *adaptively robust Kalman filter* (ARKF) with a predicted residuals-based fading factor is devised to resist the adverse influence of both dynamic model error and GNSS outliers [18]. In addition, the fading factor could also be constructed from the innovation sequence to deflate the gain matrix [19], and this robust Kalman filter could be improved with the IGG (Institute of Geodesy and Geophysics) scheme [20]. Motivated by the ARKF architecture, this paper proposes a reliable in-flight alignment for UAV's on-board MEMS-INS aided by GNSS. A rotation-based attitude determination method is devised to perform in-flight coarse alignment, overcoming the calculation burden and model switches. Moreover, the technique of the innovation-based robust Kalman filter is adopted to handle the measurement outliers. The improved in-flight initial alignment is proposed by combining both methods and applied to small UAV MEMS-based navigation. Compared with the traditional approaches, the proposed method can complete accurate initial alignment even when outliers happen. The field test results also demonstrate its effectiveness.

The structure of this paper is as follows. Section 2 briefly describes the INS error state model for in-flight alignment. Section 3 presents the derivations and implementations of the proposed in-flight alignment. The test results and conclusions are given in Section 4 and 5.

2. MEMS-INS error-state model for in-flight alignment

This paper presents an in-flight initial alignment algorithm based on the Kalman filter structure shown in Fig. 1. This section will briefly describe the core modules such as SINS mechanization, system error state model, and error compensations.

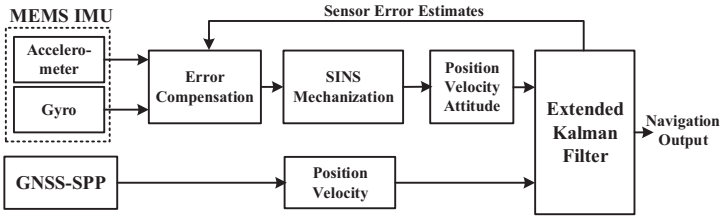

Fig. 1. The algorithm structure of in-flight alignment for MEMS-INS aided by GNSS.

2.1. SINS dynamics

As a strap-down INS, accelerometers and gyros are mounted upon the vehicle directly to sense the body motion. This kind of inertial system which may be used to navigate in the vicinity of the Earth is formulated as the Newtonian equations in the n-frame [6]:

$$\begin{cases} \dot{\boldsymbol{v}}^n = \boldsymbol{C}_b^n \boldsymbol{f}^b - (2\boldsymbol{\omega}_{ie}^n + \boldsymbol{\omega}_{en}^n) \times \boldsymbol{v}^n + \boldsymbol{g}^n \\ \dot{\boldsymbol{C}}_b^n = \boldsymbol{C}_b^n (\boldsymbol{\omega}_{ib}^b \times) - (\boldsymbol{\omega}_{in}^n \times) \boldsymbol{C}_b^n \end{cases}, \tag{1}$$

where $\boldsymbol{v}^n = [v_N, v_E, v_D]^T$ is the vehicle velocity along northern, eastern and downward directions of n-frame; $\boldsymbol{C}_b^n$ is the attitude transformation matrix from the b-frame to the n-frame; $\boldsymbol{f}^b$ is the specific force of b-frame relative to inertial frame (i-frame) resolved in b-frame measured by accelerometers, and $\boldsymbol{\omega}_{ib}^b$ is the angular rate of b-frame relative to inertial i-frame resolved in b-frame measured by gyros; $\boldsymbol{\omega}_{ie}^n$ and $\boldsymbol{\omega}_{en}^n$ are the Earth's rate and transfer rate resolved in n-frame, and $\boldsymbol{\omega}_{in}^n = \boldsymbol{\omega}_{ie}^n + \boldsymbol{\omega}_{en}^n$; $\boldsymbol{g}^n$ is the gravity vector resolved in n-frame. It indicates that these derivatives (*i.e.*, $\dot{\boldsymbol{v}}^n$ and $\dot{\boldsymbol{C}}_b^n$) are integrated to obtain estimates of vehicle velocity and attitude relative to their initial values in (1). The position can be subsequently obtained by integrating the velocity estimate. Expressed as latitude, longitude and altitude in the geodetic coordinates, *i.e.*, $\boldsymbol{r} = [L, \lambda, h]^T$, the position rate can be written as:

$$\dot{L} = v_N/(R+h), \qquad \dot{\lambda} = v_E/[(R+h)\cos L], \qquad \dot{h} = -v_D. \tag{2}$$

The strap-down computational algorithm which obtains the estimates of vehicle position, velocity and attitude by high-precision numerical integration is termed as SINS mechanization. Savage's works [21, 22] are widely recognized in such calculation, reducing the computation errors to a negligible level. As a result, it is the quality of initial alignment and the inertial sensor bias residuals that result in the growing navigation errors, which could be tackled by the proposed alignment algorithm based on a Kalman filter presented in the following parts.

2.2. System state model

The INS error-state vector consists of 15 components, *i.e.* three position errors, three velocity errors, three attitude errors, three gyro bias errors and three accelerometer bias errors. For simplicity, the dynamic state equation in the n-frame is briefly listed here. The interested readers can refer to [23] for detailed derivations.

$$\dot{\boldsymbol{x}} = \boldsymbol{F}\boldsymbol{x} + \boldsymbol{G}\boldsymbol{w}, \tag{3}$$

where $\boldsymbol{x} = [\delta\boldsymbol{r}, \delta\boldsymbol{v}, \boldsymbol{\phi}, \boldsymbol{\varepsilon}, \boldsymbol{\nabla}]^T = [\delta L, \delta\lambda, \delta h, \delta v_N, \delta v_E, \delta v_D, \phi_N, \phi_E, \phi_D, \varepsilon_X, \varepsilon_Y, \varepsilon_Z, \nabla_X, \nabla_Y, \nabla_Z]^T$ is the error state, in which δL, $\delta\lambda$ and δh represent the position errors in latitude, longitude, and

height; δv_N, δv_E, and δv_D represent the velocity errors in the north, east and downward directions; ϕ_N, ϕ_E, and ϕ_D represent misalignment angles between the computed and real attitudes; ε_X, ε_Y, and ε_Z represent the gyro bias errors; ∇_X, ∇_Y and ∇_Z represent the accelerometer bias errors. The system noise vector is defined as $\boldsymbol{w}$:

$$\boldsymbol{w} = [w_{gx}, w_{gy}, w_{gz}, w_{ax}, w_{ay}, w_{az}, \xi^b_{gx}, \xi^b_{gy}, \xi^b_{gz}, \xi^b_{ax}, \xi^b_{ay}, \xi^b_{az}]^T. \tag{4}$$

In (1), the matrices $\boldsymbol{F}$ and $\boldsymbol{G}$ are expressed as follows:

$$\boldsymbol{F} = \begin{bmatrix} \boldsymbol{F}_1 & \boldsymbol{F}_2 & \boldsymbol{0}_{3\times3} & \boldsymbol{0}_{3\times3} & \boldsymbol{0}_{3\times3} \\ \boldsymbol{F}_3 & \boldsymbol{F}_4 & \boldsymbol{F}_5 & \boldsymbol{0}_{3\times3} & -\boldsymbol{C}^n_b \\ \boldsymbol{F}_6 & \boldsymbol{F}_7 & \boldsymbol{F}_8 & \boldsymbol{C}^n_b & \boldsymbol{0}_{3\times3} \\ \boldsymbol{0}_{3\times3} & \boldsymbol{0}_{3\times3} & \boldsymbol{0}_{3\times3} & \boldsymbol{0}_{3\times3} & \boldsymbol{0}_{3\times3} \\ \boldsymbol{0}_{3\times3} & \boldsymbol{0}_{3\times3} & \boldsymbol{0}_{3\times3} & \boldsymbol{0}_{3\times3} & \boldsymbol{0}_{3\times3} \end{bmatrix}, \quad \boldsymbol{G} = \begin{bmatrix} \boldsymbol{0}_{3\times3} & \boldsymbol{0}_{3\times3} & \boldsymbol{0}_{3\times3} & \boldsymbol{0}_{3\times3} \\ \boldsymbol{0}_{3\times3} & -\boldsymbol{C}^n_b & \boldsymbol{0}_{3\times3} & \boldsymbol{0}_{3\times3} \\ \boldsymbol{C}^n_b & \boldsymbol{0}_{3\times3} & \boldsymbol{0}_{3\times3} & \boldsymbol{0}_{3\times3} \\ \boldsymbol{0}_{3\times3} & \boldsymbol{0}_{3\times3} & \boldsymbol{I}_{3\times3} & \boldsymbol{0}_{3\times3} \\ \boldsymbol{0}_{3\times3} & \boldsymbol{0}_{3\times3} & \boldsymbol{0}_{3\times3} & \boldsymbol{I}_{3\times3} \end{bmatrix}, \tag{5}$$

in which, $\boldsymbol{0}_{3\times3}$ and $\boldsymbol{I}_{3\times3}$ represent the 3×3 zero matrix and the 3×3 identity matrix, respectively;

$$\boldsymbol{F}_1 = \begin{bmatrix} 0 & 0 & -\dfrac{v_N}{R^2} \\ \dfrac{v_E \tan L}{R\cos L} & 0 & -\dfrac{v_E}{R^2\cos L} \\ 0 & 0 & 0 \end{bmatrix}, \quad \boldsymbol{F}_2 = \begin{bmatrix} \dfrac{1}{R} & 0 & 0 \\ 0 & \dfrac{1}{R\cos L} & 0 \\ 0 & 0 & -1 \end{bmatrix},$$

$$\boldsymbol{F}_3 = \begin{bmatrix} -v_E\left(2\Omega\cos L - \dfrac{v_E}{R\cos^2 L}\right) & 0 & \dfrac{1}{R^2}\left(v_E^2\tan L - v_N v_D\right) \\ 2\Omega(v_N\cos L - v_D\sin L) + \dfrac{v_N v_E}{R\cos^2 L} & 0 & -\dfrac{v_E}{R^2}\left(v_N\tan L + v_D\right) \\ 2\Omega v_E\sin L & 0 & \dfrac{1}{R^2}\left(v_N^2 + v_E^2\right) \end{bmatrix},$$

$$\boldsymbol{F}_4 = \begin{bmatrix} \dfrac{v_D}{R} & -2\Omega(\sin L + \dfrac{v_E\tan L}{R}) & \dfrac{v_N}{R} \\ 2\Omega\sin L + \dfrac{v_E}{R}\tan L & \dfrac{1}{R}(v_N\tan L + v_D) & 2\Omega\cos B + \dfrac{v_E}{R} \\ -\dfrac{2v_N}{R} & -2(\Omega\cos L + \dfrac{v_N}{R}) & 0 \end{bmatrix},$$

$$\boldsymbol{F}_5 = \begin{bmatrix} 0 & -f_D & f_E \\ f_D & 0 & -f_N \\ -f_E & f_N & 0 \end{bmatrix}, \quad \boldsymbol{F}_6 = \begin{bmatrix} -\Omega\sin L & 0 & -\dfrac{v_E}{R^2} \\ 0 & 0 & \dfrac{v_N}{R^2} \\ -\Omega\cos L - \dfrac{v_E}{R\cos^2 L} & 0 & \dfrac{v_E\tan L}{R^2} \end{bmatrix},$$

$$\boldsymbol{F}_7 = \begin{bmatrix} 0 & \dfrac{1}{R} & 0 \\ -\dfrac{1}{R} & 0 & 0 \\ 0 & -\dfrac{\tan L}{R} & 0 \end{bmatrix}, \quad \boldsymbol{F}_8 = \begin{bmatrix} 0 & -\Omega\sin L - \dfrac{v_E\tan L}{R} & \dfrac{v_N}{R} \\ \Omega\sin L + \dfrac{v_E\tan L}{R} & 0 & \Omega\cos L + \dfrac{v_E}{R} \\ -\dfrac{v_N}{R} & -\Omega\cos L - \dfrac{v_E}{R} & 0 \end{bmatrix},$$

where Ω is the Earth's rate; f_N, f_E, and f_D are the measured specific forces resolved in the n-frame, *i.e.* $\boldsymbol{f}^n = \boldsymbol{C}^n_b \boldsymbol{f}^b$; R is the Earth radius.

2.3. System observation model

Both GNSS and INS can output position and velocity components when GNSS positioning is available. So the position and velocity differences between GNSS and INS can be taken as the observations, *i.e.* $\boldsymbol{Z} = [\boldsymbol{r}_{INS} - \boldsymbol{r}_{GNSS}, \boldsymbol{v}_{INS} - \boldsymbol{v}_{GNSS}]^T$.

The lever-arm $\boldsymbol{\ell}_G^b$ is defined as a vector from the INS centre to the GNSS antenna phase centre referenced in the b-frame. The corresponding observation equation is:

$$\boldsymbol{Z} = \boldsymbol{H}\boldsymbol{x} + \boldsymbol{e}. \tag{6}$$

The measurement matrix $\boldsymbol{H}$ and the noise vector $\boldsymbol{e}$ are defined as:

$$\boldsymbol{H} = \begin{bmatrix} \boldsymbol{I}_{3\times3} & \boldsymbol{0}_{3\times3} & (\boldsymbol{C}_b^n\boldsymbol{\ell}_G^b)\times & \boldsymbol{0}_{3\times3} & \boldsymbol{0}_{3\times3} \\ \boldsymbol{0}_{3\times3} & \boldsymbol{I}_{3\times3} & -[(\boldsymbol{\omega}_{in}^n\times)(\boldsymbol{C}_b^n\boldsymbol{\ell}_G^b\times) + \boldsymbol{C}_b^n(\boldsymbol{\ell}_G^b \times \boldsymbol{\omega}_{ib}^b)\times] & -\boldsymbol{C}_b^n(\boldsymbol{\ell}_G^b\times) & \boldsymbol{0}_{3\times3} \end{bmatrix},$$
$$\boldsymbol{e} = \begin{bmatrix} \boldsymbol{e}_r \\ \boldsymbol{e}_v \end{bmatrix}, \tag{7}$$

where the symbol '$(\cdot)\times$' denotes the skew symmetric matrix constructed by the vector elements in the brackets. Usually, the GNSS data rate is far less than that of INS, *e.g.* 1 Hz as the typical value. The state-space model of GNSS/INS integrated system is constituted by the Equations (3) and (6).

2.4. Error compensations

When GNSS solutions are available at $\boldsymbol{t}_k$ moment, the INS predicted navigation error state (a priori estimate) is $\boldsymbol{x}_k^- = [\delta\boldsymbol{r}_k^-, \delta\boldsymbol{v}_k^-, \boldsymbol{\phi}_k^-, \boldsymbol{\varepsilon}_k^-, \boldsymbol{\nabla}_k^-]^T$, and the updated error state (a posteriori estimate) is $\boldsymbol{x}_k^+ = [\delta\boldsymbol{r}_k^+, \delta\boldsymbol{v}_k^+, \boldsymbol{\phi}_k^+, \boldsymbol{\varepsilon}_k^+, \boldsymbol{\nabla}_k^+]^T$. The updated errors will be used to calibrate the inertial sensors and update the navigation results. The INS predicted position $\boldsymbol{r}_k^-$ and velocity $\boldsymbol{v}_k^-$ can be compensated as follows:

$$\boldsymbol{r}_k^+ = \boldsymbol{r}_k^- - \delta\boldsymbol{r}_k^+, \qquad \boldsymbol{v}_k^+ = \boldsymbol{v}_k^- - \delta\boldsymbol{v}_k^+. \tag{8}$$

Based on the assumption of small misalignment angles, the INS predicted attitude matrix $\boldsymbol{C}_{b,k}^{n-}$ is rectified as:

$$\boldsymbol{C}_{b,k}^{n+} = (I + [\boldsymbol{\phi}_k^+\times])\boldsymbol{C}_{b,k}^{n-}. \tag{9}$$

The INS predicted gyro bias $\boldsymbol{b}_{gyro,k}^-$ and accelerometer bias $\boldsymbol{b}_{accl,k}^-$ are corrected as:

$$\boldsymbol{b}_{gyro,k}^+ = \boldsymbol{b}_{gyro,k}^- + \boldsymbol{\varepsilon}_k^+, \qquad \boldsymbol{b}_{accl,k}^+ = \boldsymbol{b}_{accl,k}^- + \boldsymbol{\nabla}_k^+, \tag{10}$$

where the a posteriori estimates $\boldsymbol{b}_{gyro,k}^+$ and $\boldsymbol{b}_{accl,k}^+$ represent the inertial sensor biases at $\boldsymbol{t}_k$ moment, and they could be used to correct raw inertial measurements (*i.e.*, $\widetilde{\boldsymbol{\omega}}_{ib,k}^b$ and $\widetilde{\boldsymbol{f}}_k^b$) at $\boldsymbol{t}_k$ moment:

$$\hat{\boldsymbol{\omega}}_{ib,k}^b = \widetilde{\boldsymbol{\omega}}_{ib,k}^b - \boldsymbol{\varepsilon}_k^+, \qquad \hat{\boldsymbol{f}}_k^b = \widetilde{\boldsymbol{f}}_k^b - \boldsymbol{\nabla}_k^+. \tag{11}$$

The calibrated measurements (*i.e.*, $\hat{\boldsymbol{\omega}}_{ib,k}^b$ and $\hat{\boldsymbol{f}}_k^b$) will be used for SINS mechanization.

3. Improved in-flight alignment for MEMS-based INS in UAV applications

The improved in-flight initial alignment can be divided into two stages, *i.e.* coarse alignment and fine alignment. The in-flight coarse alignment provides a sound initial attitude with the accuracy of a few degrees for the following fine alignment. For flying UAVs, the proposed in-flight coarse alignment can determine a rough initial attitude aided by a single GNSS antenna, without the need of additional external aids, such as a magnetometer or multi-GNSS antennas. Guaranteed by the coarse alignment, the improved fine alignment can be achieved with a robust Kalman filter to reduce the effects of GNSS outliers.

3.1. Improvement with in-flight coarse alignment

To determine the rough initial attitude of a moving body, we proposed a novel in-flight coarse alignment method based on the rotation vector [3]. This approach aims at accomplishing attitude initialization during UAV flight, and is demonstrated by the field test. In the following part, the algorithm is presented briefly and the readers can refer to [3] for details.

The proposed in-flight coarse alignment is devised to obtain the initial attitude quaternion q_b^n by two consecutive rotations, as shown in Fig. 2. The corresponding quaternions to the first and second rotations are denoted as $\boldsymbol{q}_b^f$ and $\boldsymbol{q}_f^n$, respectively. The initial attitude can be determined as $\boldsymbol{q}_b^n = \boldsymbol{q}_b^f \circ \boldsymbol{q}_f^n$, *i.e.*:

$$\boldsymbol{f}^{n0} = \boldsymbol{q}_b^n * \circ \boldsymbol{f}^{b0} \circ \boldsymbol{q}_b^n, \tag{12}$$

where $\boldsymbol{f}^{b0}$ and $\boldsymbol{f}^{n0}$ are the unitization vectors of $\boldsymbol{f}^b$ and $\boldsymbol{f}^n$, *i.e.*:

$$\boldsymbol{f}^{n0} = \boldsymbol{f}^n / \|\boldsymbol{f}^n\|, \qquad \boldsymbol{f}^{b0} = \boldsymbol{f}^b / \left\|\boldsymbol{f}^b\right\|, \tag{13}$$

where $\|\cdot\|$ represents the norm of a vector.

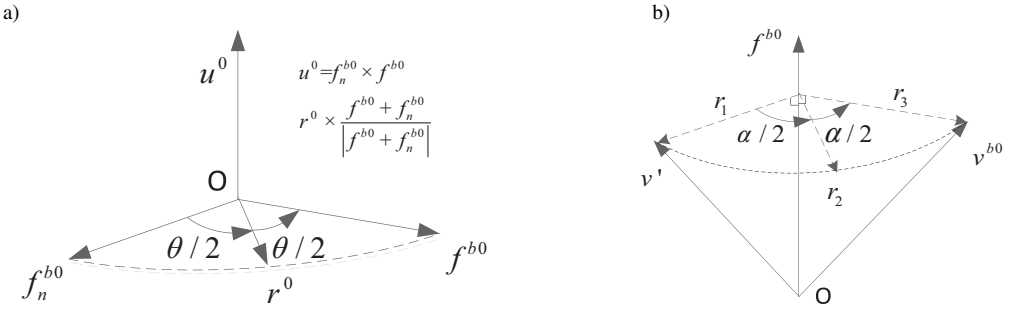

Fig. 2. The coarse attitude determination with two consecutive rotations. The first rotation process (a); the second rotation process (b).

Equation (1) shows that $\boldsymbol{f}^n$ can be constructed as:

$$\boldsymbol{f}^n = \dot{\boldsymbol{v}}^n + (2\boldsymbol{\omega}_{ie}^n + \boldsymbol{\omega}_{en}^n) \times \boldsymbol{v}^n - \boldsymbol{g}^n, \tag{14}$$

where $\dot{\boldsymbol{v}}^n$ is the body total acceleration in n-frame, which can be approximated by the velocity difference between two consecutive GNSS moments, *i.e.* average acceleration in n-frame.

For the first rotation, the vector triad $\left(\boldsymbol{f}^{n0}, \boldsymbol{v}^{n0}, \boldsymbol{f}^{n0} \times \boldsymbol{v}^{n0}\right)$ rotates by the angle θ around $\boldsymbol{f}^{n0} \times \boldsymbol{f}^{b0}$, as shown in Fig. 2a. The corresponding quaternion $\boldsymbol{q}_b^f$ is computed as:

$$\begin{cases} \boldsymbol{r}^0 = \dfrac{\boldsymbol{f}^{b0} + \boldsymbol{f}^{n0}}{\left\|\boldsymbol{f}^{b0} + \boldsymbol{f}^{n0}\right\|}, \qquad \boldsymbol{u}^0 = \dfrac{\boldsymbol{f}^{n0} \times \boldsymbol{r}^0}{\left\|\boldsymbol{f}^{n0} \times \boldsymbol{r}^0\right\|} \\ \sin\left(\dfrac{\theta}{2}\right) = \left\|\boldsymbol{f}^{n0} \times \boldsymbol{r}^0\right\|, \qquad \cos\left(\dfrac{\theta}{2}\right) = \sqrt{1 - \sin^2\left(\dfrac{\theta}{2}\right)} \\ \boldsymbol{q}_b^f = \cos\left(\dfrac{\theta}{2}\right) + \boldsymbol{u}^0 \cdot \sin\left(\dfrac{\theta}{2}\right) \end{cases}. \tag{15}$$

The first rotation transforms $\boldsymbol{v}^{n0}$ into a new vector $\boldsymbol{v}'$, *i.e.*:

$$\boldsymbol{v}^{n0} = \boldsymbol{v}^n / \left\|\boldsymbol{v}^n\right\|, \qquad \boldsymbol{v}' = \boldsymbol{q}_b^f * \circ \boldsymbol{v}^{n0} \circ \boldsymbol{q}_b^f. \tag{16}$$

Then, a newly-formed vector triad $\left(\boldsymbol{f}^{b0}, \boldsymbol{v}', \boldsymbol{f}^{b0} \times \boldsymbol{v}'\right)$ rotates by the angle α around $\boldsymbol{f}^{b0}$, as shown in Fig. 2b. Assuming the sideslip rate ρ_{slip} can be known with some special sensor (*e.g.* ρ_{slip} is set to zero in a balanced flight), the analytical solution of $\boldsymbol{v}^{b0} = [v_x, \rho_{slip}, v_z]^T$ can be obtained by the motion constraints of UAV [3]:

$$\begin{cases} c = \boldsymbol{f}^{b0} \cdot (\boldsymbol{q}_b^f * \circ \boldsymbol{v}^{n0} \circ \boldsymbol{q}_b^f) - f_y \cdot \rho_{slip} \\ v_x = \left\{f_x \cdot c + |f_z| \cdot \left[(f_x^2 + f_z^2) \cdot (1 - \rho_{slip}^2) - c^2\right]^{1/2}\right\} / (f_x^2 + f_z^2) \\ v_y = \rho_{slip} \\ v_z = c - f_x \cdot v_x / f_z \end{cases}, \tag{17}$$

where $\boldsymbol{f}^{b0} = [f_x, f_y, f_z]^T$. The corresponding quaternion $\boldsymbol{q}_f^n$ to the second rotation is computed as:

$$\begin{cases} \boldsymbol{r}_1 = \boldsymbol{v}' - \boldsymbol{v}' \cdot \boldsymbol{f}^{b0}, \qquad \boldsymbol{v}^{b0} = \boldsymbol{v}^b / \left\|\boldsymbol{v}^b\right\| \\ \boldsymbol{r}_3 = \boldsymbol{v}^{b0} - \boldsymbol{v}^{b0} \cdot \boldsymbol{f}^{b0}, \qquad \boldsymbol{r}_2 = \boldsymbol{r}_1 + \boldsymbol{r}_3 \\ \boldsymbol{r}_1^0 = \boldsymbol{r}_1 / \left\|\boldsymbol{r}_1\right\|, \qquad \boldsymbol{r}_2^0 = \boldsymbol{r}_2 / \left\|\boldsymbol{r}_2\right\| \\ \sin\left(\dfrac{\alpha}{2}\right) = \left(\boldsymbol{r}_1^0 \times \boldsymbol{r}_2^0\right) \cdot \boldsymbol{f}^{b0}, \qquad \cos\left(\dfrac{\alpha}{2}\right) = \sqrt{1 - \sin^2\left(\dfrac{\alpha}{2}\right)} \\ \boldsymbol{q}_f^n = \cos\left(\dfrac{\alpha}{2}\right) + \boldsymbol{f}^{b0} \cdot \sin\left(\dfrac{\alpha}{2}\right) \end{cases}. \tag{18}$$

Finally, the initial attitude is computed as:

$$\boldsymbol{q}_b^n = \boldsymbol{q}_b^f \circ \boldsymbol{q}_f^n. \tag{19}$$

Subsection 4.2 will compare this method with its traditional counterpart by the field test.

3.2. Improved Robust Kalman filtering for in-flight fine alignment

Based on the sound initial state provided by in-flight coarse alignment, the discretization and linearization can be performed. The state equation and measurement equation are discretized to construct extended Kalman filter.

$$\begin{cases} \boldsymbol{x}_k = \boldsymbol{\Phi}_{k,k-1} \boldsymbol{x}_{k-1} + \boldsymbol{\Gamma}_{k,k-1} \boldsymbol{w}_{k-1} \\ \boldsymbol{Z}_k = \boldsymbol{H}_k \boldsymbol{x}_k + \boldsymbol{e}_k \end{cases}, \tag{20}$$

where $\boldsymbol{x}_k$ is the error state at time k; $\boldsymbol{\Phi}_{k,k-1}$ is the state transition matrix from time $k-1$ to time k; $\boldsymbol{\Gamma}_{k,k-1}$ is the noise design matrix; the system noise vector at time $k-1$ is $\boldsymbol{w}_{k-1} \sim N(\boldsymbol{0}, \boldsymbol{Q}_{k-1})$, $\boldsymbol{H}_k$ is the measurement design matrix at time k; and $\boldsymbol{e}_k$ is the measurement noise vector with the covariance matrix $\boldsymbol{R}_k$.

Using the SINS error model as accurate system dynamics, the KF innovation $\boldsymbol{v}_k = \boldsymbol{Z}_k - \boldsymbol{H}_k \boldsymbol{x}_k^-$ can reflect the effects of GNSS observation outliers. For the discretized system depicted by (20), the innovation sequence $\left\{\boldsymbol{v}_k = \boldsymbol{Z}_k - \boldsymbol{H}_k \boldsymbol{x}_k^-\right\}$ should satisfy the following property:

$$\begin{cases} E\left[\boldsymbol{v}_k\right] = 0, \quad \forall k \\ E\left\{\boldsymbol{v}_k \boldsymbol{v}_j^T\right\} = \boldsymbol{C}_k \delta_{kj}, \qquad \boldsymbol{C}_k = \boldsymbol{H}_k \boldsymbol{P}_k^- \boldsymbol{H}_k^T + \boldsymbol{R}_k \end{cases}, \tag{21}$$

where δ_{kj} is the Kronecker function. If the actual model structures and parameters are consistent with (20), (21) will hold true. On the contrary, if (21) is violated, it is reasonable to judge that some improper approximations or outliers exist. In GNSS/INS integration, the hypothesis test can be performed to check whether the actual GNSS observation violates the model assumptions, in which the null hypothesis is $\boldsymbol{v}_k \sim N(\boldsymbol{0}, \boldsymbol{C}_k)$. As a judging index for observation outlier detection, the test statistics γ_k is constructed as:

$$\gamma_k = M_k^2 = \boldsymbol{v}_k \boldsymbol{C}_k^{-1} \boldsymbol{v}_k^T, \tag{22}$$

where $M_k = \sqrt{\left(\boldsymbol{Z}_k - \boldsymbol{H}_k \boldsymbol{x}_k^-\right)^T \boldsymbol{C}_k^{-1} \left(\boldsymbol{Z}_k - \boldsymbol{H}_k \boldsymbol{x}_k^-\right)}$ is the Mahalanobis distance [19]. If the null hypothesis holds, the test statistics obeys the Chi-square distribution $\chi^2(m)$ with the degree of freedom m. The probability threshold of rejection for the null hypothesis, *i.e.* the significance level α, should be of a very small value, *e.g.* 0.01%. With this judging index, the null hypothesis can be rejected if the computed value is larger than the Chi-square α-quantile $\chi_\alpha^2(m)$, meaning that either actual measurements are not compatible with the assumed model or outliers are detected. In other words, the above test process can be written as:

$$Pr\left\{\gamma_k > \chi_\alpha^2(m)\right\} = \alpha, \tag{23}$$

where $Pr(\cdot)$ represents the probability of a random event. The (23) indicates $\gamma_k > \chi_\alpha^2(m)$ as an event of small probability. When this event happens, it is reasonable to reject the null hypothesis and conclude that outliers are detected.

To resist the adverse influence of outliers, a scaling factor λ_k is constructed based on γ_k and $\chi_\alpha^2(m)$ to devise a robust Kalman filter. If the computed γ_k is larger than $\chi_\alpha^2(m)$, the adaptive factor λ_k is introduced to inflate the innovation covariance $\boldsymbol{C}_k$:

$$\overline{\boldsymbol{C}}_k = \lambda_k \boldsymbol{C}_k. \tag{24}$$

Thus, the following equation should be satisfied:

$$\gamma_k = \boldsymbol{v}_k \overline{\boldsymbol{C}}_k^{-1} \boldsymbol{v}_k^T = \chi_\alpha^2(m). \tag{25}$$

Then

$$\lambda_k = \begin{cases} 1 & \gamma_k \le \chi_\alpha^2(m) \\ \dfrac{\gamma_k}{\chi_\alpha^2(m)} & \gamma_k > \chi_\alpha^2(m) \end{cases}. \tag{26}$$

Equation (26) is the analytical solution of adaptive factor λ_k without an iterative process as employed in [19]. When an observation outlier occurs, the factor $\lambda_k > 1$ will reduce the gain $\boldsymbol{K}_k$ to balance the contribution of observations in state estimation. It can be observed that the robust KF is transformed to a standard KF when there is no outlier detected with $\lambda_k = 1$.

3.3. Implementation of proposed in-flight initial alignment

Implementation of the proposed reliable in-flight alignment approach is obtained by combining Subsection 3.1 and Subsection 3.2, and listed briefly as follows.

Step 1: Initialization of the navigation filter:

(1) The initial position and velocity are set as the GNSS-derived solutions ($\boldsymbol{r}_{GNSS}$ and $\boldsymbol{v}_{GNSS}$).

(2) The initial attitude $\boldsymbol{q}_b^n$ is obtained by the proposed in-flight coarse alignment algorithm with the GNSS velocity ($\boldsymbol{v}_{k-1}^n, \boldsymbol{v}_k^n$) and accelerometer measurements ($\boldsymbol{f}_{k-1}^b, \boldsymbol{f}_k^b$) at two consecutive GNSS moments t_{k-1} and t_k, according to (12)~(19).

(3) The error state $\boldsymbol{x}_0^+$ is set to zero, and the corresponding covariance $\boldsymbol{P}_0^+$ is a diagonal matrix $diag(\sigma_L^2, \sigma_\lambda^2, \sigma_h^2, \sigma_{v_N}^2, \sigma_{v_E}^2, \sigma_{v_D}^2, \sigma_{\phi_N}^2, \sigma_{\phi_E}^2, \sigma_{\phi_D}^2, \sigma_{\varepsilon_X}^2, \sigma_{\varepsilon_Y}^2, \sigma_{\varepsilon_Z}^2, \sigma_{\nabla_X}^2, \sigma_{\nabla_Y}^2, \sigma_{\nabla_Z}^2)$. Some diagonal elements are set by experience with $\sigma_L = \sigma_\lambda = \frac{\sqrt{2}}{2}\sigma_h = 5$ m, $\sigma_{v_N} = \sigma_{v_E} = \frac{\sqrt{2}}{2}\sigma_{v_D} = 0.1$ m/s, $\sigma_{\phi_N} = \sigma_{\phi_E} = \sigma_{\phi_D} = 0.2$ rad; and the elements $\sigma_{\varepsilon_X} = \sigma_{\varepsilon_Y} = \sigma_{\varepsilon_Z} = 4 \times 10^{-3}$ rad/s and $\sigma_{\nabla_X} = \sigma_{\nabla_Y} = \sigma_{\nabla_Z} = 3 \times 10^{-2}$ m/s^2 are set according to noise parameters included in Table 1.

Step 2: SINS mechanization:

Equations (1) and (2) are numerically integrated for SINS-predicted position, velocity and attitude estimates, using the corrected inertial measurements $\hat{\boldsymbol{\omega}}_{ib,k}^b$ and $\hat{\boldsymbol{f}}_k^b$ from (11);

Step 3: Time update:

$$\boldsymbol{x}_k^- = \boldsymbol{\Phi}_{k,k-1}\boldsymbol{x}_{k-1}^+, \qquad \boldsymbol{P}_k^- = \boldsymbol{\Phi}_{k,k-1}\boldsymbol{P}_{k-1}^+\boldsymbol{\Phi}_{k,k-1}^T + \boldsymbol{\Gamma}_{k,k-1}\boldsymbol{Q}_{k-1}\boldsymbol{\Gamma}_{k,k-1}^T. \tag{27}$$

Step 4: Computation of the innovation vector and its covariance:

$$\boldsymbol{v}_k = \boldsymbol{Z}_k - \boldsymbol{H}_k\boldsymbol{x}_k^-, \qquad \boldsymbol{C}_k = \boldsymbol{H}_k\boldsymbol{P}_k^-\boldsymbol{H}_k^T + \boldsymbol{R}_k. \tag{28}$$

Step 5: The test statistics $\widetilde{\gamma}_k$ is calculated with (20), and the factor λ_k is updated with (24);

Step 6: Measurement update:

$$\boldsymbol{K}_k = \lambda_k^{-1}\boldsymbol{P}_k^-\boldsymbol{H}_k^T(\boldsymbol{H}_k\boldsymbol{P}_k^-\boldsymbol{H}_k^T + \boldsymbol{R}_k)^{-1}. \tag{29}$$

$$\boldsymbol{x}_k^+ = \boldsymbol{x}_k^- + \boldsymbol{K}_k(z_k - \boldsymbol{H}_k\boldsymbol{x}_k^-), \qquad \boldsymbol{P}_k^+ = (\boldsymbol{I} - \boldsymbol{K}_k\boldsymbol{H}_k)\boldsymbol{P}_k^-(\boldsymbol{I} - \boldsymbol{K}_k\boldsymbol{H}_k)^T + \boldsymbol{K}_k\boldsymbol{R}_k\boldsymbol{K}_k^T. \tag{30}$$

Step 7: Error compensation with (8), (9) and (10);

Return to Step 2 until the end of the whole flight.

4. Field test

4.1. Test setup

A field test was performed with the GNSS/MEMS-INS integrated prototype system, as shown in Fig. 3 (middle), mounted on a small UAV. The prototype system consists of a low-cost MEMS-based IMU (ADIS14605) and a GNSS receiver. The IMU is used for collecting inertial data with the noise parameters listed in Table 1. The GNSS receiver is used for collecting GNSS data. The field test airborne equipment is shown in Fig. 3 (left). The airborne MEMS-INS performs the in-flight alignment aided by GNSS *single point positioning* (SPP), *i.e.* SPP position and velocity. Intentionally, a temporary GNSS base station as shown in Fig. 3 (right) was installed on the top of the Aerospace Engineering building at the university premises, to obtain the centimetre-level

Table 1. ADIS16405 IMU noise parameters.

Parameter type	Gyro	Accelerometer
Bias	3.0 deg/sec	50 mg
Bias Instability	0.007 deg/sec	0.2 mg
Random Walk	2.0 deg/$\sqrt{\text{hr}}$	0.2 m/sec/$\sqrt{\text{hr}}$

Fig. 3. The airborne equipment (left), GNSS/MEMS-INS prototype system (middle), and RTK base station (right).

real-time kinematic (RTK) results as the position reference. Therefore, the alignment performance can be reflected by the position error. The test site is located in the open area on the Moon Island, about 10 km away from the base station.

The UAV RTK reference trajectory is presented in Fig. 4, which shows that the circular movement is the main manoeuvre to guarantee the filter state observability. It takes about 15~20 min for IMU warm-up, then the in-flight initial alignment begins once the UAV takes off.

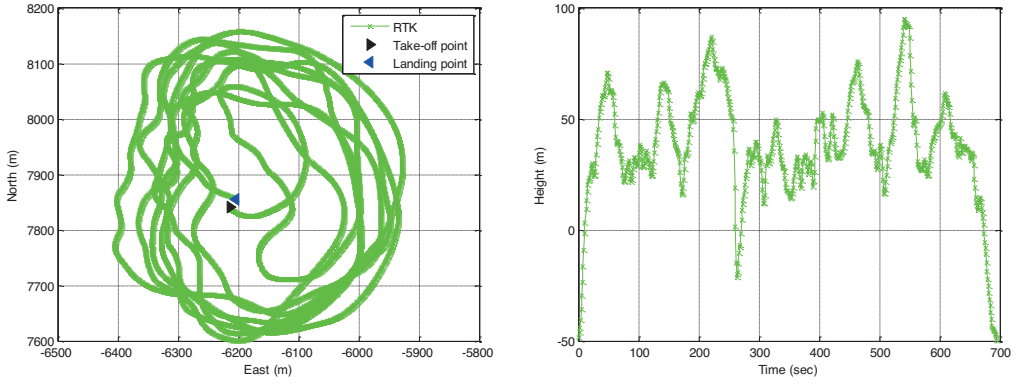

Fig. 4. The horizontal trajectory (left) and the vertical position (right) of UAV flight.

4.2. In-flight coarse alignment results

The proposed coarse alignment algorithm and the conventional method [14] are compared here. The Kalman filter attitude estimates are used as the reference. Both coarse alignment algorithms are executed at every moment during the whole flight, and Fig. 5 shows their attitude errors. It can be noticed that the proposed algorithm with a known sideslip (green dashed line) significantly improves the accuracy of attitude estimation, compared with other methods. In fact,

the zero-sideslip simplified algorithm (red dotted line) also greatly enhances the roll estimation accuracy and slightly improves the yaw estimation, compared with the traditional method (blue solid line). Fig. 5 also shows that the blue and red lines encounter some large disturbances in heading and pitch angles, which are caused by the actual sideslip of UAV, thus violating the zero-sideslip assumption. If the lateral speed can be measured by some special sensor, it is demonstrated that the proposed algorithm with known sideslip (green dashed line) will never undergo such disturbances. The *root mean square errors* (RMSE) of these three algorithms are listed in Table 2, which indicates that the proposed coarse alignment algorithm provides a better attitude estimate. The accuracy enhancement is benefited from the combined use of both GNSS and INS measurements, while the conventional algorithm uses only the single GNSS antenna observations. It will also be demonstrated that the proposed in-flight coarse alignment can provide a sound initial value for the following fine alignment.

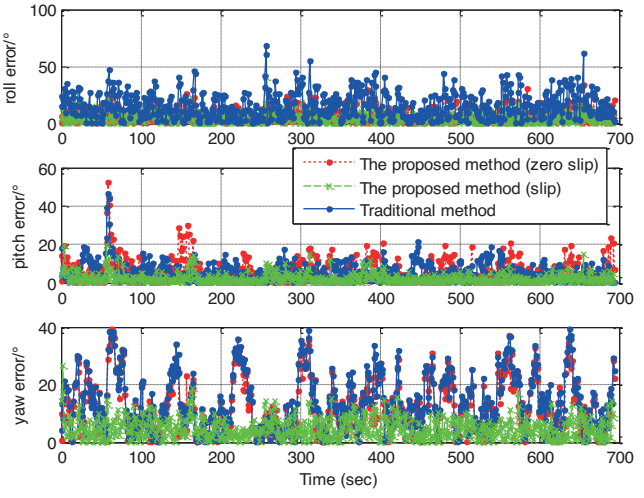

Fig. 5. Comparison of the in-flight coarse attitude error for the proposed and traditional algorithms.

Table 2. Comparison of the coarse alignment accuracy for the proposed and traditional algorithms.

Algorithm type	Roll RMSE [deg]	Pitch RMSE [deg]	Yaw RMSE [deg]
Traditional method	19.0510	7.2999	16.7469
The proposed method (zero slip assumption)	9.0040	8.3487	15.4732
The proposed method (non-zero slip)	7.0862	3.5584	6.0682

4.3. In-flight fine alignment results

Because Satellite 16 is observable during the whole test, an outlier of 100m is given to the C/A-code observation of Satellite 16 every 100 moments to test the proposed algorithm. Fig. 6 (left) shows the SPP position error characteristics in this situation. Fig. 6 (left) also shows that the average number of observable satellites is about 6 during the flight test, and the PDOP (position dilution of precision) reflects the changing satellite geometry with the number of satellites.

In Fig. 6 (left), the outlier occurrence moments are marked by red arrows, and GNSS position outliers also occur at the corresponding moments.

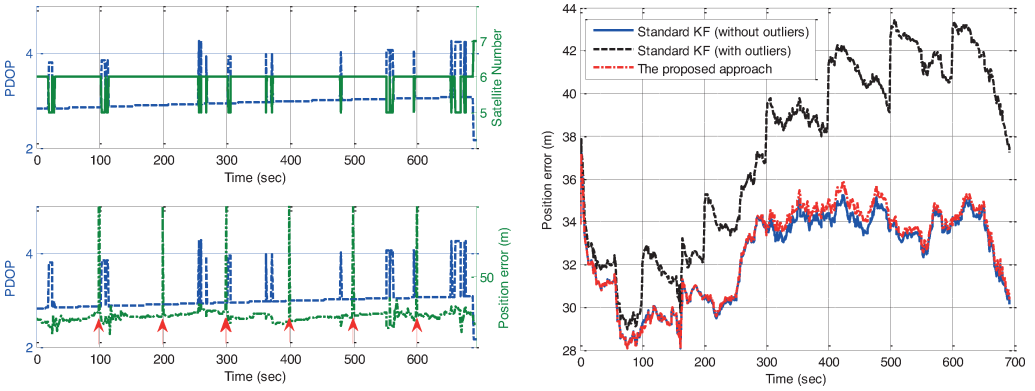

Fig. 6. A posteriori analysis of the GNSS SPP error (left) and comparison of position errors for different algorithms in three case studies (right).

Based on the in-flight coarse alignment result at first moment, three fine alignment cases are analysed and compared here.

Case 1: Fine alignment scheme uses standard KF without introducing outliers;

Case 2: Fine alignment scheme uses standard KF with outliers every 100 moments;

Case 3: Fine alignment scheme uses the robust KF with outliers every 100 moments.

Figure 6 (right) shows the position error of each scheme. It can be observed that the blue solid line shows the standard KF performance without observation outliers, while the black dashed line corresponds to the results with outliers introduced every 100 moments. It should be noticed that the standard KF suffers from outliers, resulting in a degraded performance during the fine alignment. On the other hand, Fig. 6 (right) shows that the red dot-and-dash line is very close to the blue solid line even in the case of GNSS outliers. Table 3 shows the *root-mean-square errors* (RMSE) of both standard KF and robust KF in the presence of outliers after the fine alignment almost stabilizes. It can be seen that the adoption of robust KF significantly improves the overall accuracy by 15% and by more than 50% the accuracy in horizontal directions, compared with the traditional fine alignment using the standard KF.

Table 3. Fine alignment accuracy of the proposed and conventional algorithms in the case of outliers.

Algorithm type	North position RMSE [m]	East position RMSE [m]	Downward position RMSE [m]	Position RMSE norm [m]
Standard KF	24.01	6.54	32.41	40.86
The proposed approach	10.21	3.44	32.46	34.20

The comparison between Fig. 6 (left) and Fig. 6 (right) indicates that the GNSS position outliers in Fig. 6 (left) contribute to the divergence of conventional fine alignment at corresponding moments in Fig. 6 (right), while the proposed robust method still performs well at these moments. This fact demonstrates that the proposed robust method can complete fine alignment in a way that is immune from observation outliers, resulting in an improved alignment accuracy.

5. Conclusions

In this paper, a novel two-stage in-flight initial alignment approach is proposed for the airborne MEMS-based INS aided by GNSS. In order to address the attitude estimation in a moving base, a real-time in-flight coarse alignment algorithm adopts accurate GNSS velocity and acceleration sensed by IMU to construct the nonlinear equation of initial attitude, and its approximate solution is derived with the devised two-rotation method. The in-flight fine alignment overcomes the adverse influence of observation outliers on the alignment performance using innovation filtering. The field test results have demonstrated that the proposed algorithm can improve the in-flight alignment accuracy even when the observations are contaminated by outliers, compared with conventional methods.

References

[1] Bento, M.F. (2008). Unmanned Aerial Vehicles: An Overview. *InsideGNSS*, 1, 54–61.

[2] Schmidt, G.T. (2015). Navigation sensors and systems in GNSS degraded and denied environments. *Chinese Journal of Aeronautics*, 28, 1–10.

[3] Wang, D.J., Chen, L., Wu, J. (2016). Novel In-flight coarse alignment of low-cost Strapdown Inertial Navigation System for Unmanned Aerial Vehicle Applications. *Transactions of The Japan Society for Aeronautical and Space Sciences*, 59(1), 10–17.

[4] Shin, E.H., Naser E.S. (2007). Unscented Kalman Filter and Attitude Errors of Low-Cost Inertial Navigation Systems. *Navigation, Journal of the Institute of Navigation*, 54(1), 1–9.

[5] Han, S.L., Wang, J.L. (2010). A novel initial alignment scheme for low-cost INS aided by GPS for land vehicle applications. *The Journal of Navigation*, 63(4), 663–680.

[6] Groves, P.D. (2008). *Principles of GNSS, inertial and multisensor integrated navigation systems*. London: Artech House, 407–418.

[7] Kong, X. (2004). INS algorithm using quaternion model for low cost IMU. *Robotics and Autonomous Systems*, 46(4), 221–246.

[8] Wang, D.J., Lv H.F., Wu, J. (2017). In-flight Alignment for small UAV MEMS-based navigation via adaptive unscented Kalman filtering approach. *Aerospace Science and Technology*, 61, 73–84.

[9] Wang, D.J., Lv, H.F., Wu, J. (2016). Augmented Cubature Kalman Filter for nonlinear RTK/MIMU Integrated Navigation with non-additive noise. *Measurement*, 97, 111–125.

[10] Rogers, R.M. (1997). IMU In-Motion Alignment without Benefit of Attitude Initialization. *Navigation, Journal of the Institute of Navigation*, 44(3), 301–311.

[11] Wu, M.P., Wu, Y.X., Hu, X.P., Hu, D.W. (2011). Optimization-based alignment for inertial navigation systems: Theory and algorithm. *Aerospace Science and Technology*, 15(1), 1–17.

[12] Wu, Y.X., Pan, X.F. (2013). Velocity/Position Integration Formula Part I: Application to In-Flight Coarse Alignment. *IEEE Transactions on Aerospace and Electronic Systems*, 49(2), 1006–1023.

[13] Ma, L., Wang, K., Shao, M. (2013). Initial alignment on moving base using GPS measurements to construct new vectors. *Measurement*, 46(8), 2405–2410.

[14] Richard, P.K., Hansman R.J., John, D. (1998). Single-antenna GPS-based aircraft attitude determination. *Navigation, Journal of the Institute of Navigation*, 45(1), 51–60.

[15] Wieser, A., Fritz, B.K. (2002). Short static GPS Sessions: robust estimation results. *GPS Solution*, 76(6), 353–358.

[16] Wang, J.L., Wang, J. (2007). Mitigating the effect of multiple outliers on GNSS navigation with M-estimation schemes. *Proc. of International Global Navigation Satellite Systems Society Symposium 2007*, Sydney, Australia, 1–9.

[17] Tong, H.B., Zhang, G.Z. (2014). Robust positioning algorithm with modified M-estimation for multiple outliers. *Acta Geodaetica et Cartographica Sinica*, 43(4), 366–371.

[18] Wu, F.M., Yang, Y.X. (2010). An extended adaptive Kalman filtering in tight coupled GPS/INS integration. *Survey Review*, 42(316), 146–154.

[19] Chang, G.B. (2014). Robust Kalman filtering based on Mahalanobis distance as outlier judging criterion. *Journal of Geodesy*, 88, 391–401.

[20] Li, Z.K., Wang, J., Gao, J.X. (2017). Application of improved robust Kalman filter in data fusion for PPP/INS tightly coupled positioning system. *Metrol. Meas. Syst*., 24(2), 289–301.

[21] Savage, P.G. (1998). Strapdown inertial navigation integration algorithm design Part 1: attitude algorithms. *Journal of Guidance, Control, and Dynamics*, 21(1), 19–28.

[22] Savage, P.G. (1998). Strapdown inertial navigation integration algorithm design Part 2: velocity and position algorithms. *Journal of Guidance, Control, and Dynamics*, 21(2), 208–221.

[23] Quinchia, A.G., Falco, G., Falletti, E., Dovis, F., Ferrer, C. (2013). A comparison between different error modeling of MEMS applied to GPS/INS integrated systems. *Sensors*, 13, 9549–9588.